





RESEARCH ARTICLE

Posture Dependence of Cerebral Spinal Fluid and Blood Flow by Phase Contrast Magnetic Resonance Imaging at 3 T

¹School of Biomedical Engineering & State key Laboratory of Advanced Medical Materials and Devices, ShanghaiTech University, Shanghai, China | ²United Imaging Healthcare, Shanghai, China | ³Shanghai Clinical Research and Trial Center, Shanghai, China

Correspondence: Xiaopeng Zong (zongxp@shanghaitech.edu.cn)

Received: 18 June 2025 | Revised: 7 September 2025 | Accepted: 22 September 2025

Funding: The authors received no specific funding for this work.

Keywords: automatic slice positioning | blood flow | cerebrospinal fluid | phase-contrast MRI | posture dependence | prospective motion correction

ABSTRACT

Understanding how body posture influence the cerebrospinal fluid (CSF) and blood flow is crucial for developing effective treatment strategies for neurological diseases. 2D phase contrast (PC) MRI is commonly used to investigate flow dynamics in the cerebral aqueduct (CAq) and large blood vessels. However, the measured results are susceptible to head motion and variation in slice locations between postures.

We developed a PC-MRI sequence incorporating prospective motion correction (PMC) and consistent slice prescription. Using this sequence, we investigated blood and CSF dynamics in young healthy adults in supine and prone postures. Stroke volumes, flow velocities, absolute flows, and cross-sectional areas of the CAq, internal carotid artery (ICA), vertebral artery, internal jugular vein (IJV), superior sagittal sinus, and straight sinus were measured in 14 healthy volunteers in both postures.

Compared to the supine posture, we found no significant change in blood flow in any blood vessels in the prone posture, but the ICA (p=0.009) and IJV (p=0.049) stroke volume significantly decreased. Meanwhile, the absolute flow (p=0.005), stroke volume (p=0.001), and velocity variation range $V_{\rm range}(p$ =0.002) of the CAq significantly decreased in the prone posture. There were significant positive correlations between the posture-induced stroke volume changes of CAq and ICA (p=0.55, p=0.044) and of IJV and ICA (p=0.76, p=0.016). The cardiac phase dependent changes in flow velocities were also strongly correlated between CAq and ICA.

These findings suggest a close coupling between blood flow and CSF dynamics and a reduction of CSF circulation during prone posture. The developed sequence will facilitate longitudinal monitoring of vascular and CSF flow properties during the pathogenesis of neurovascular diseases.

1 | Introduction

Disturbances in cerebral hemodynamics and cerebrospinal fluid (CSF) dynamics are associated with neurological disorders such as stroke and hydrocephalus [1–3]. Therefore, understanding the factors that modulate hemodynamic and CSF behavior may shed new light on the pathogenesis of these conditions. A variety

of physiological and behavioral factors have been shown to influence these dynamics, including respiration [4–8], cardiac pulsation [9], blood pressure [10, 11], neural activity [12], physical movement [13], and body posture [14]. Among these factors, body posture has drawn growing attention for its influence on fluid physiology in the human body. Postural changes have been shown to affect a range of physiological processes, including

© 2025 John Wiley & Sons Ltd.

blood and CSF circulation, heart rate regulation, blood pressure modulation, and adaptive responses of the autonomic nervous system [14–26].

Supine and prone positions are among the most common postures in daily life and are also frequently adopted in clinical interventions and rehabilitation. For example, prone positioning has been widely applied in the treatment of severe respiratory diseases [27], whereas long-term bedridden patients are typically maintained in the supine posture. Previous studies have shown that CSF circulation is enhanced during sleep, facilitating the clearance of metabolic waste [28, 29], and posture may influence this process. Therefore, comparing CSF and blood flow dynamics between supine and prone positions is not only important for understanding the regulatory mechanisms of posture on brain waste clearance but also has implications for disease management and clinical neuroimaging applications.

However, studies that simultaneously assess the effects of posture on human CSF dynamics, blood flow, and their coupling are still lacking. Previous studies have primarily focused on examining changes in CSF or blood flow between the upright and supine postures [17, 20], or only on comparing blood flow changes between the supine and prone postures [23].

The phase-contrast magnetic resonance imaging (PC-MRI) sequence is a well-established noninvasive technique for measuring blood and CSF flow [30-33]. By targeting specific vessels, placing the imaging plane perpendicular to the vessels, and setting the velocity encoding gradient parallel to the vessels, 2D PC-MRI requires less scan time and allows dynamic properties to be measured within a few minutes compared to the 4D counterpart [34]. However, if the imaging slice is not perpendicular to the blood vessel, the measured flow velocity may be underestimated. In addition, measured velocity can vary depending on the slice location along the vessels [35]. Therefore, to accurately assess the posture dependence, it is essential to ensure that the same anatomical location is scanned across different postures. Moreover, involuntary head movements resulting from prolonged posture maintenance (particularly in the prone posture) may introduce motion artifacts, which can in turn affect the accuracy of flow measurements [36-38].

This study aims to measure CSF and blood flow dynamics at cerebral aqueduct (CAq), vertebral arteries (VAs), internal carotid arteries (ICAs), internal jugular veins (IJVs), superior sagittal sinus (SSS), and straight sinus (SRS) in the supine and prone postures in young healthy adults. To ensure consistent slice placement across supine and prone postures, a consistent slice prescription method was developed based on image registration. As the CAq is typically curved, to ensure that the imaging slice was perpendicular to the CAq, the slice position and orientation were calculated based on CAq masks automatically segmented using a 3D U-Net [39]. Furthermore, to reduce motion artifacts caused by involuntary head movements, we implemented fat navigator (FatNav)-based prospective motion correction (PMC) for the PC-MRI sequence. The proposed approach is also suitable for longitudinal studies, as it enables consistent slice positioning across repeated scans.

The Methods and Results sections are each divided into two parts. The first part describes the development and validation of the slice prescription and PMC methods, and the second part reports the study of the posture dependence of CSF and blood flow dynamics in CAq and large cerebral blood vessels.

2 | Methods

All studies were approved by the Ethics Committee of ShanghaiTech University. Informed written consent was obtained from each subject prior to MRI scans.

2.1 | Technical Development

2.1.1 | CAq Segmentation and Slice Prescription

Because of the curved shape of the CAq, manual slice prescription was time-consuming and susceptible to human errors. Therefore, we first developed a 3D U-Net based CAq segmentation model to automatically generate CAq masks based on 3D T2-weighted images (T2WI), which allowed automatic and accurate determination of the slice position and orientation.

2.1.1.1 | Data Acquisition for Segmentation Model Development. Twenty-nine subjects (aged 20–47 years; 8 females, 21 males) were scanned using a variable flip angle turbo spin echo (TSE) sequence to obtain T2WI for training a 3D U-Net model for automatic CAq segmentation. Some of them underwent multiple scans using identical or different protocols, resulting in a total of 61 T2WI. The sequence parameters are summarized in Table 1.

2.1.1.2 | Segmentation Model Training and Testing. All T2WI data were cropped to a matrix size of 128×128×128 whose center coincided with the center of CAq before input into a 3D U-Net model for CAq segmentation [39]. Representative cropped T2WI slices for training and testing are shown in the left column of Figure 1. The U-Net architecture is given in Figure 1S. The ground truth CAq mask was manually labeled from the bottom of the third ventricle to the top of the fourth ventricle, as shown in the middle column of Figure 1.

The segmentation accuracy was evaluated using 10-fold cross-validation by randomly dividing all subjects into 10 groups (1 group with 2 subjects and the remaining 9 with 3 subjects each). The training was repeated 10 times with each of the 10 groups serving as the test set while the remaining nine serving as the training set. Model performance was assessed using three standard metrics: dice similarity coefficient (DSC), sensitivity (SEN), and positive predictive value (PPV), defined as follows:

$$DSC = \frac{2TP}{2TP + FP + FN} \tag{1}$$

$$SEN = \frac{TP}{TP + FN}$$
 (2)

$$PPV = \frac{TP}{TP + FP} \tag{3}$$

TABLE 1 | The parameters of the turbo spin echo sequence for obtaining T2 weighted images.

Protocols	1	2	3	4	
FOV (mm3)	$256 \times 240 \times 208$	$336 \times 329 \times 270$	$256 \times 246 \times 200$	$320 \times 300 \times 208$	
Voxel size (mm3)	$0.80 \times 0.80 \times 0.80$	$0.6 \times 0.6 \times 0.6$	$0.8 \times 0.8 \times 0.8$	$0.80\times0.80\times0.80$	
TR/TE (ms)	3200/569.6	3000/408	3000/401.72	3200/569.6	
Flip angle (°)	21~180	22~180	22~180	21~180	
Accel factor	3.11	5	6	3.83	
No. averages	1	1	7	1	
Scan time (min:sd)	3:35	5:57	19:00	4:09	
No. subjects	14	24	15	8	

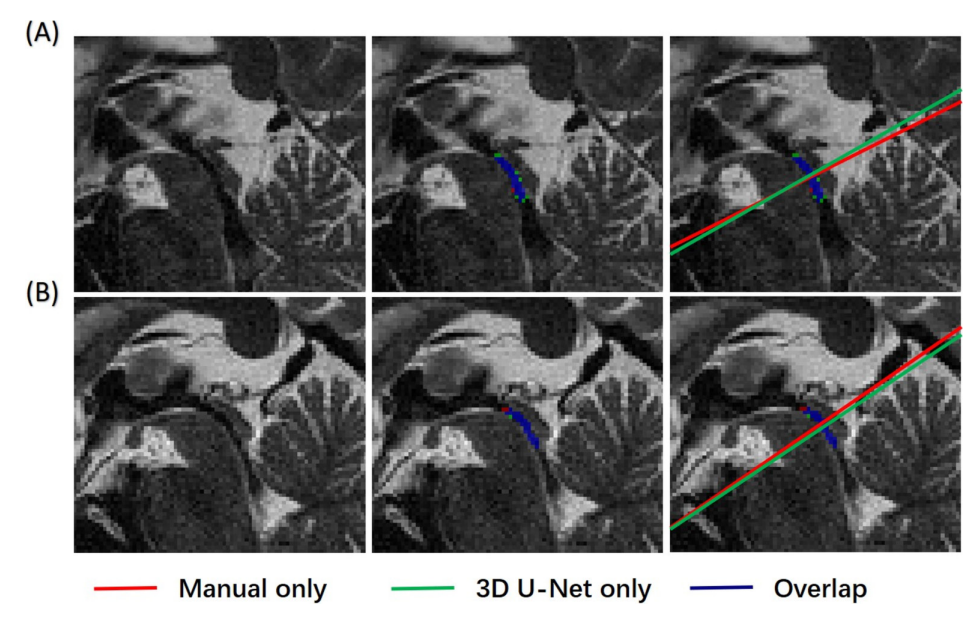


FIGURE 1 | (A) and (B) representative T2-weighted images cropped to a matrix size of $128 \times 128 \times 128$ in two subjects. The cropped region centered on the CAq and was used for training and testing the 3D U-Net model. The middle column shows overlaid manual and U-Net predicted segmentation masks, while the right column shows the manual and calculated slice prescriptions.

where TP, FP, and FN represent true positive, false positive, and false negative voxel counts, respectively, using the manually annotated CAq mask as ground truth.

2.1.1.3 | Slice Prescription. Based on the manually or automatically segmented CAq masks, the following procedure was adopted to obtain the slice prescription. First, the terminal points of the CAq masks were identified using their 3D coordinates. Then, the shortest centerline path in the mask that connects these two points was obtained using the shortestpath function in MatLab. The midpoint of this path was selected as the center of the scan plane. Finally, to determine the orientation of the CAq path, we selected nine voxels including the middle voxel of the path and four voxels above and four voxels below the middle voxel along the path. Principal component analysis (PCA) was then applied to the coordinates of these nine voxels, and the first principal component was taken as the slice normal direction. We estimated the maximum deviation of the estimated direction from the true direction as the rotation angle

around the center which gives rise to a relative displacement of one voxel between the two terminals of the nine voxels segment. Therefore, the error is calculated to be $\arctan(1/9)=6^\circ$, which was used in Section 2.1.2.1 to measure the effect of slice direction change on the measured flow velocity. The T2WI reconstruction took $\sim\!60\,\mathrm{s}$. The CAq segmentation and scan slice calculation took $10\,\mathrm{s}$ on a workstation equipped with i9-13900K CPU and 128 Gigabytes of memory. The workstation was separate from the scanner.

2.1.2 | Consistent Slice Prescription After Repositioning

To ensure consistent slice position relative to the head after head movement, the slice position of the first scan was used to calculate that of the following scans using a spatial transformation matrix obtained by registering the T2WI at the new position to the T2WI at the first position. To validate the effectiveness of

NMR in Biomedicine, 2025 3 of 18

the developed slice prescription method, the flow parameters of CAq were repeatedly measured in 12 healthy volunteers (aged 24–27 years; 2 females, 10 males) with and without subject repositioning. Then, the repeatabilities of the parameters were compared between the repositioning and no repositioning conditions. The subjects remained in the supine posture during all scans in this section.

2.1.2.1 | **Data Acquisition.** The initial slice position was automatically determined based on the segmented CAq mask from the T2WI obtained prior to the PC-MRI scans, as detailed in Section 2.1.1. The T2W1 sequence parameters are shown in the first column of Table 1 and the PC sequence parameters are shown in the first column of Table 2.

Subsequently, two consecutive PC-MRI scans were performed without subject repositioning as a reference. To evaluate whether slight deviations in the slice angle would affect measured flow, 10 of the participants underwent additional one or two scans, during which the imaging plane was rotated by 6° in the sagittal plane from the original orientation.

Afterwards, 8 of the subjects were asked to exit the scanner and rested for 5 min. They then re-entered the scanner in the supine posture, and the slice position was recalculated using spatial transformation matrices obtained by registering the reacquired T2WI to the initial T2WI using the registration module in the Insight toolkit (ITK) (v4.6) [40, 41]. The registration module was integrated into the PC-MRI scan preparation software such that no manual input of the new slice positions was needed. Last, one or two scans were performed in the new slice positions. Participants were instructed to remain still during all scans.

2.1.2.2 | Data Analysis

2.1.2.2.1 | **Image Consistency After Repositioning.** All data analysis was performed offline. To quantitatively assess the consistency of repeated scan positioning, we calculated the Structural Similarity Index (SSIM) [42] between the images obtained from the first and second scans before repositioning, and between the first images before and after repositioning.

2.1.2.2.2 | **Reconstruction of Dynamic PC Images.** All PC-MRI k-space data were divided into 10 cardiac phases

according to their acquisition time in the cardiac cycle. Data in each cardiac cycle were reconstructed using the GRAPPA algorithm [43], resulting in 10×2 (2 consists of velocity encoding gradient on and off) images. We found that increasing the number of phases would lead to ring-like vessels in the reconstructed images in some phases, due to a higher undersampling factor with an increased number of phases.

The magnitude images of individual coils were combined by root sum of squares, and the phase images were calculated from the phase of the summed products of the complex images with velocity encoding gradient on and the complex conjugate of the image with VENC off of individual coils [44].

2.1.2.2.3 | Definition of CAq and Background ROIs. CAq ROIs were defined using a threshold-based method. As shown in Figure 2S (A), a background ROI was defined as a ring immediately surrounding the CAq with a width of four pixels, and the vessel ROIs were identified as pixels within the ring with intensities two standard deviations above the mean in the magnitude image, where the standard deviation and mean were calculated in the background ROI. The vessel ROIs were defined based on the magnitude images averaged across all cardiac phases. After generating the ROIs, isolated pixels were removed to ensure spatial continuity of ROIs.

2.1.2.2.4 | **Background Phase Correction.** To mitigate phase errors induced by eddy currents, background phase was estimated by fitting the phase image in the background ROIs with a second-order polynomial. The estimated background phase was then subtracted from the phase image [45].

2.1.2.2.5 | **Flow Parameters.** Quantitative measures were derived from the dynamic flow velocity curves, including absolute flow (F_{abs}) , cross-sectional area, and velocity range (V_{range}) [46, 47], as follows:

$$F_{abs} = \frac{1}{n} \sum_{i=1}^{n} |V_i| S$$
 (4)

where V_i and S are the velocity of each cardiac phase i and cross-sectional area, respectively, and n is the number of cardiac phases. The cross-sectional area was calculated the product of the number of pixels in the vessel ROIs and square of in-plane

TABLE 2 | The parameters of TOF and PC-MRI sequences.

		PC			
Sequence	PC (CAq)	(VA, ICA, IJV, SSS, SRS)	TOF		
FOV	$210 \times 180 (\text{mm}^2)$	$220 \times 180 (\text{mm}^2)$	$250 \times 190 \times 36.8 (\text{mm}^3)$		
Voxel size (mm3)	$0.66 \times 0.66 \times 5$	$0.49 \times 0.49 \times 2$	$0.49 \times 0.49 \times 0.80$		
TR/TE (ms)	60/15	60/15	35/7		
Flip angle (°)	25	50	20		
No. averages	20	20	1		
Accel factor	2	2	5.04		
VENC (cm/s)	15	90/60	N/A		
Scan time (min:sd)	3:04	3:59	5:11		

pixel size. $V_{\rm range}$ was calculated as the difference between the maximum and minimum velocities. The minimal and maximum positions in the velocity time courses were determined on the group-averaged velocity time courses, as their determination was susceptible to errors due to the presence of noise in individual time courses.

To quantify repeatability, the coefficient of repeatability was calculated as

Coefficient of Repeatability =
$$1.96 * \sigma_d$$
, (5)

where σ_d is the standard deviation of differences between repeated measurements. The repeatability of $V_{\rm range}$ and $F_{\rm abs}$ of CSF within the CAq was evaluated using the Bland–Altman plot, comparing continuous scanning without and with repositioning. Furthermore, changes in $V_{\rm range}$ and $F_{\rm abs}$ were calculated after changing the slice orientation by 6° .

2.1.3 | FatNav-Based PMC

PMC was developed for the PC-MRI sequence to reduce motion artifacts in images. PMC is achieved by adjusting the position and direction of the imaging field of view (FOV) in real-time based on motion parameters measured using FatNavs, to ensure consistent slice position relative to the head. To evaluate the effectiveness of PMC, flow parameters were compared between conditions of still, head motion without PMC, and head motion with PMC. The evaluation was only performed for the CAq, SSS, and SRS, as our pilot study found that PMC was not effective for cervical vessels ICA, VA, and IJV.

2.1.3.1 | **Data Acquisition.** The FatNav and PC-MRI data were acquired in an interleaved manner, similar to what has been reported before [48]. The FatNav acquisition parameters were as follows: matrix size = $56 \times 56 \times 56$, FOV = $224 \times 224 \times 224 \times 224 \times mm^3$, TE = 2.8 ms, TR = 5.0 ms, partial

Fourier factor = 0.8 along both phase and partition encoding directions, acceleration factor = 4×4 , flip angle = 7° . The initial FatNav image was continuously acquired at the beginning of the sequence with a TR of 5 ms, obtaining fully sampled calibration data from the 24×24 (PE×PAR) central rectangular region of k-space, so the acquisition time of the initial FatNav image was 3.3 s. The subsequent FatNav volumes (121 lines each) were interleaved into the PC-MRI sequence by distributing the acquisition across multiple PC-MRI TRs. Since the FatNav was applied during the blank period of the main sequence, the TR of the PC-MRI did not increase, so the acquisition time of subsequent FatNav volumes is 3.63 s. Therefore, the total scan time increase is only ~3.3 s compared to the standard PC-MRI sequence.

To investigate the potential effects of the FatNav and PMC modules on flow quantification, 12 participants (aged 19–24 years; 4 females, 8 males) were scanned with their heads remaining still. Three PC-MRI scans were conducted to measure the cardiac phase dependent flow of CAq or blood vessels, including a conventional PC-MRI without FatNav or PMC, a PC-MRI with FatNav but no PMC, and a PC-MRI with FatNav and PMC.

Each participant was first scanned by TSE and time-of-flight (TOF) sequences for CAq and blood vessel visualization. The slice prescription method of CAq was the same as in Section 2.1.2.1, and for other vessels, the slice positions were manually determined by placing the slices approximately perpendicular to the VA/ICA/IJV and SSS/SRS on the TOF and T2WI, respectively. The yellow lines in Figure 2 indicate the slice positions for the different vessels. The PC and TOF sequence parameters are provided in Table 2.

To assess the effectiveness of the PMC module for alleviating motion artifacts, 18 participants (aged 23–27 years, 4 females, 14 males) were instructed to perform head rotations without moving their eyes to follow the movement of a fixation

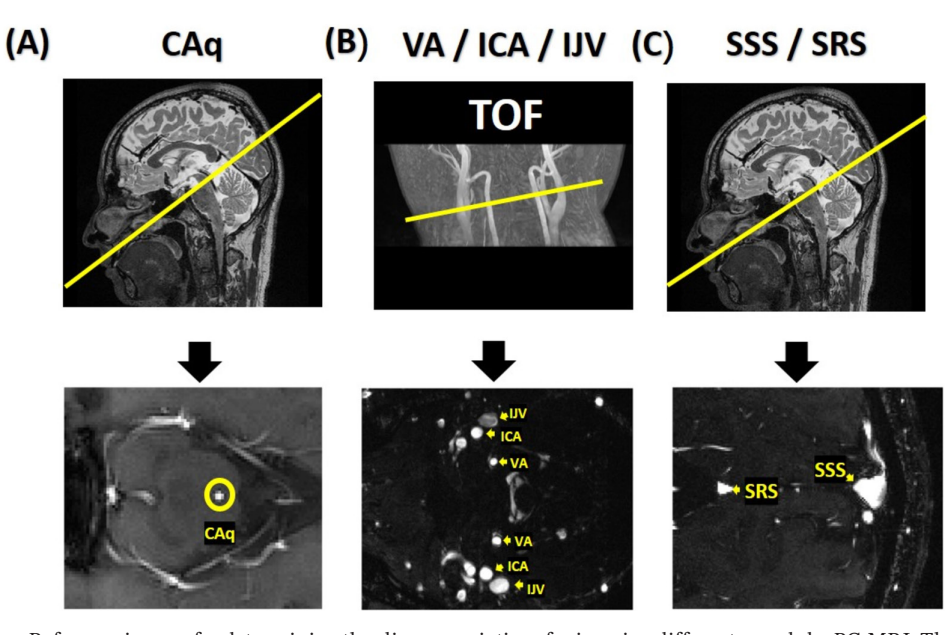


FIGURE 2 | Top row: Reference images for determining the slice prescriptions for imaging different vessels by PC-MRI. The yellow lines indicate the slice locations for the phase contrast scans. Bottom row: magnitude images from the phase contrast scans.

NMR in Biomedicine, 2025 5 of 18

mark displayed on an MR-compatible screen inside the scanner. Participants were asked to perform the same movements during scans with and without PMC. The fixation mark and their motion patterns are illustrated in Supplementary Material Figure 3S (A)–(C), which corresponds to roll, pitch, and yaw, respectively. For reference, scans were also performed with their heads remaining still and PMC off. Participants performed one to three of the motion patterns displayed in Figure 3S with PMC on and off. The subjects remained in the supine posture during all scans.

2.1.3.2 | Image Reconstruction and Processing. FatNav images were reconstructed in real-time via an extension module provided by the vendor using the GRAPPA algorithm [48, 49]. The reconstruction time of the first and subsequent FatNav images was 4.17 and 0.69s, respectively. The GRAPPA calibration kernel was calculated from the fully sampled central regions of the first FatNav image. The second FatNav image was used as a reference for registration, as the first image had slightly different contrast. Registration was carried out using ITK [40], which took about 0.5s for each FatNav image. The motion parameter reception by the sequence occurred within 70 ms after the completion of image registration. The cumulative processing time, including image reconstruction (0.69s), registration (0.5s), and parameter transmission (70 ms), totaled approximately 1.26s.

For the PC images, the reconstruction procedure is the same as described in 2.1.2.2.

2.1.3.3 | **Data Analysis.** The definition of blood vessel and background ROIs followed the same procedure as for the CAq ROIs. Unlike CAq, other vessels were present next to SSS and SRS, which could be included in the background ROI. To remove nearby vessels from the background ROI, background pixels with velocities exceeding 7 cm/s were excluded [45]. The resulting blood vessel and background ROIs are shown in Figure 2S (B)–(F). Background phase was also estimated and subtracted from the vessel phase following the same procedure as for CAq in Section 2.1.2.2. If fewer than six background pixels were available after exclusion, the mean background value was used instead.

The impacts of the FatNav and PMC on PC images were evaluated using visual assessment and quantitative measures including $F_{\rm abs}$ and $V_{\rm range}$ and mean velocity across cardiac cycle. As the velocity of CAq exhibits bipolar oscillation, only $V_{\rm range}$ was calculated for CAq, while only mean velocity across cardiac cycle was calculated for SSS and SRS.

The impact of FatNav acquisition was evaluated by comparing the results obtained under (1) PC-MRI without FatNav or PMC, (2) PC-MRI with FatNav but without PMC, and (3) PC-MRI with both FatNav and PMC conditions, when the subjects remained still. To evaluate the motion correction performance, we compared the $F_{\rm abs}$, $V_{\rm range}$, and mean velocity between PMC on and off conditions in the presence of motion. The statistical significance of the differences between conditions were assessed using the Wilcoxon signed rank test.

To assess whether the motion severity was positively correlated with its impact on the measured parameters, we calculated the absolute relative changes of the parameters under motion and PMC off conditions. The relative changes were calculated as the differences between the motion and PMC off conditions and the still condition, normalized by the values under the still condition. The motion severity was quantified by the motion score, which is defined as the sum of the root sum of squares of the translational parameter ranges (in mm) and the root sum of squares of the rotational parameter ranges (in degrees) during the whole scan.

2.2 | Posture Dependence

This section applied the techniques developed in Section 2.1 to study the CSF flow and blood flow dynamics in CAq and blood vessels under supine and prone postures.

2.2.1 | Data Acquisition

Fourteen healthy adults (aged 24–27 years; 5 females) participated in the study. Each participant was first scanned by TSE and TOF sequences for CAq and blood vessel visualization in the supine posture. The initial slice positioning methods for CAq and the blood vessels are the same as described in Section 2.1.1 and 2.1.3. Three PC-MRI scans were then acquired that targeted CAq, VA/ICA/IJV, and SSS/SRS, respectively. Participants got off the bed and rested for 5 min after completing the supine scans, then proceeded with the prone scans . A T2WI was first acquired using the same TSE sequence. The slice positions for the CAq, VA/ICA/IJV, and SSS/SRS in the prone posture were automatically calculated using spatial transformation matrices obtained by registering the T2WI in the prone posture to that in the supine posture. The registration took approximately 8 s.

For the supine position, subjects lay flat on their backs. While in the prone position, a sponge cushion was placed under the forehead to ensure unobstructed breathing, with the neck kept either straight or slightly tilted when necessary to avoid pressing the nose and arms kept straight by the side of the body, as illustrated in Figure 4S.

2.2.2 | Data Analysis

The image reconstruction and processing followed the same procedures as described in Sections 2.1.2 and 2.1.3. However, the width of the annulus for the background ROIs of ICA, IJV, and VA was two pixels, as numerous other vessels were present in close proximity.

To investigate the impact of posture on CSF and blood flow, $F_{\rm abs}$, heart rate, stroke volume, mean velocity, $V_{\rm range}$, and area of the different vessels were compared between the supine and prone postures. The Wilcoxon signed rank tests were used to assess the statistical significance of the differences in physiological and hemodynamic parameters between the postures. Furthermore,

the correlations of posture induced changes in stroke volume between different vessels were evaluated using scatter plots and Spearman correlation analysis.

3 | Results

3.1 | Technical Development

3.1.1 | CAq Segmentation and Slice Prescription

The middle columns in Figure 1 show a comparison between the manually and automatically segmented masks of the CAq in two subjects. There is a close match between the manual and automatically generated CAq masks in both subjects. Notably, these images were not included in the training of the segmentation model.

DSC of 0.90 ± 0.16 , SEN of 0.89 ± 0.02 , and PPV of 0.91 ± 0.04 (mean \pm standard deviation) were achieved in 10-fold cross validation. The average distance between the slice centers and the average angle between the slice normal directions calculated based on the manual and automatic masks were $0.61\pm0.34\,\mathrm{mm}$ and $2.33^\circ\pm0.52$, respectively.

3.1.2 | Slice Prescription After Repositioning

Figure 3A and B show representative magnitude images from PC-MRI before and after repositioning. The acquired images after repositioning exhibit high similarity to the initial images.

The SSIM between the first scan, repeated scans without repositioning and with repositioning were 0.996 ± 0.002 and 0.994 ± 0.003 , respectively.

Figure 4 presents the Bland–Altman plots for $F_{\rm abs}$ and $V_{\rm range}$ within CAq from repeated scans without and with repositioning. As shown in Figure 4A and B, the mean difference in $F_{\rm abs}$ between the two scans without and with repositioning was $-0.054\,\rm mL/min$ and $0.51\,\rm mL/min$, with a coefficient of repeatability of $1.70\,\rm mL/min$ and $1.35\,\rm mL/min$, respectively. For $V_{\rm range}$, the mean difference was $0.02\,\rm cm/s$ and $0.86\,\rm cm/s$, without and with repositioning, respectively, with the same coefficient of repeatability of $2.25\,\rm cm/s$, as shown in Figure 4C and D.

Based on 11 datasets from 10 participants, the 6° deviation in slice orientation resulted in changes of $-0.11\pm0.77\,\mathrm{mL/min}$ (-2.6% \pm 11%, p>0.05) in F_{abs} and 0.14 \pm 1.17 cm/s (-2.7% \pm 14%, p>0.05) in V_{range} . The absolute changes in F_{abs} and V_{range} were 0.6 \pm 0.4 mL/min (9% \pm 8%) and 0.8 \pm 0.8 cm/s (8% \pm 11%), respectively.

3.1.3 | FatNav-Based PMC

Our pilot study found no clear improvement in vessel clarity for VA/ICA/IJV with PMC in the presence of motion, as shown in Figure 5S. The corresponding motion traces are shown in Figures 6S and 7S, where the head motion ranges were similar between the PMC-on and PMC-off conditions.

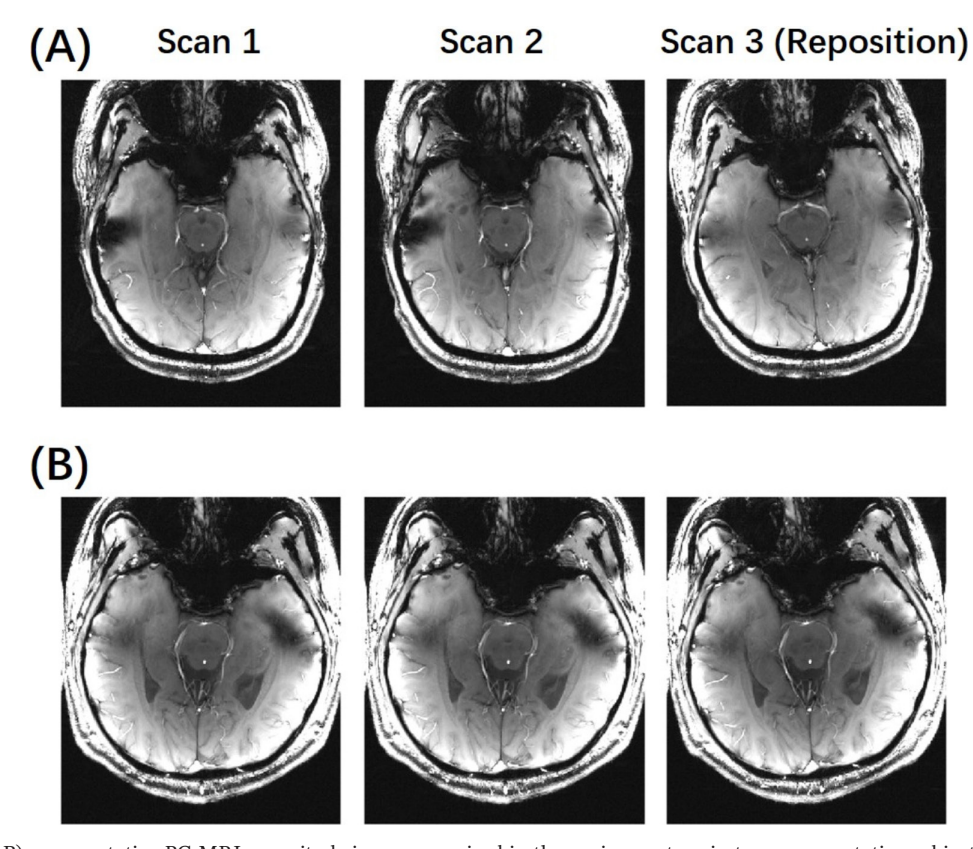


FIGURE 3 | (A–B) representative PC-MRI magnitude images acquired in the supine posture in two representative subjects. Scans 1 and 2 were obtained consecutively without repositioning, while Scan 3 was acquired after repositioning.

NMR in Biomedicine, 2025 7 of 18

Figures 5A and 6A present representative phase and magnitude images with FatNav off, FatNav on but PMC off, and PMC on, respectively, under the head still condition. In the latter two conditions, the FatNav module detected minimal motion, with a mean translational range of 0.17 mm and 0.23 mm and a mean

rotational range of 0.17° and 0.21° [48] for CAq and SSS/SRS, respectively. Visually, the background signal appeared comparable across all three conditions, with no notable artifacts. The SSIM values of magnitude images confirmed high similarity between the images: 0.9997 ± 0.0001 (CAq) and 0.9994 ± 0.0001

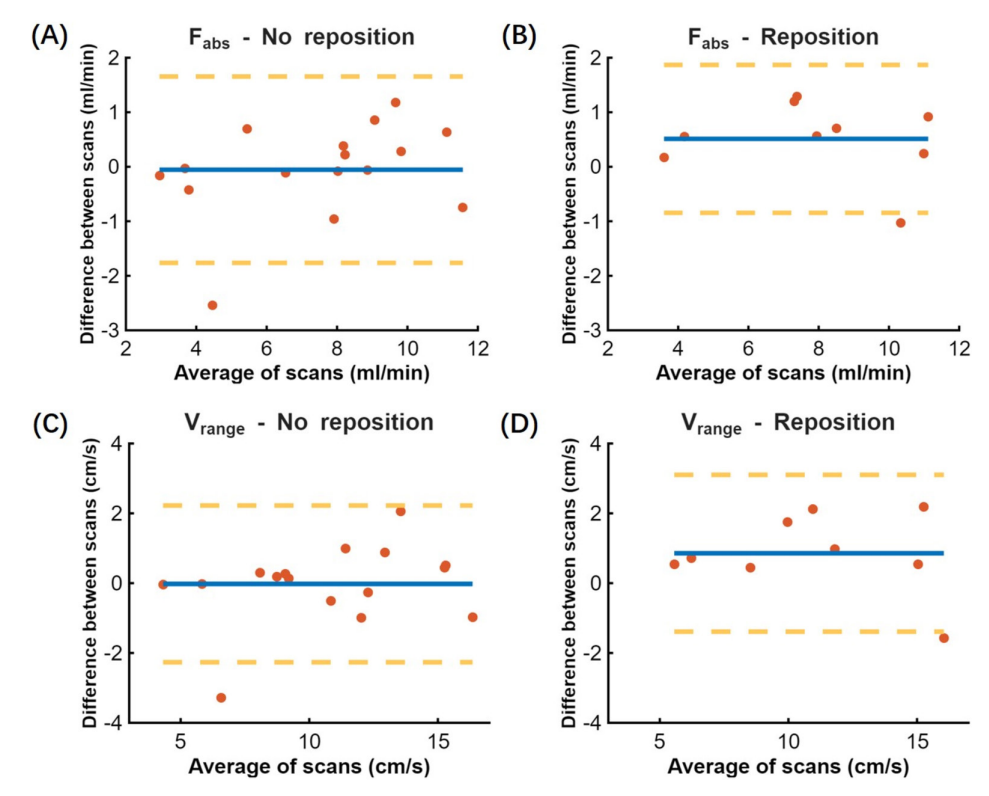


FIGURE 4 | Bland–Altman plots for F_{abs} and V_{range} in the CAq. (A) and (B) show plots of F_{abs} without and with repositioning, while (C) and (D) show plots of V_{range} .

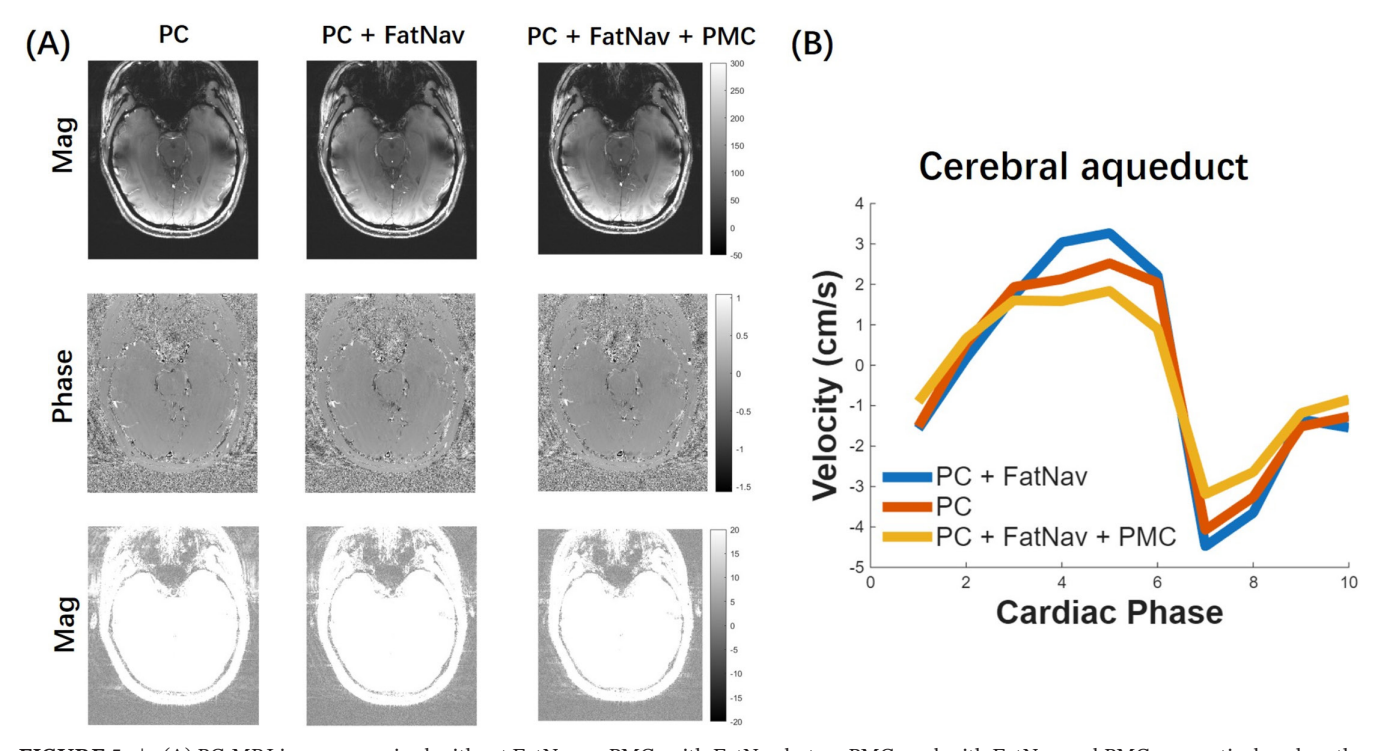


FIGURE 5 | (A) PC-MRI images acquired without FatNav or PMC, with FatNav but no PMC, and with FatNav and PMC, respectively, when the head remained still. Top two rows show representative magnitude and phase images. Third row shows magnitude images with adjusted intensity window to highlight ghosting artifacts in the background. (B) CSF velocity waveforms in the CAq under the three FatNav and PMC settings.

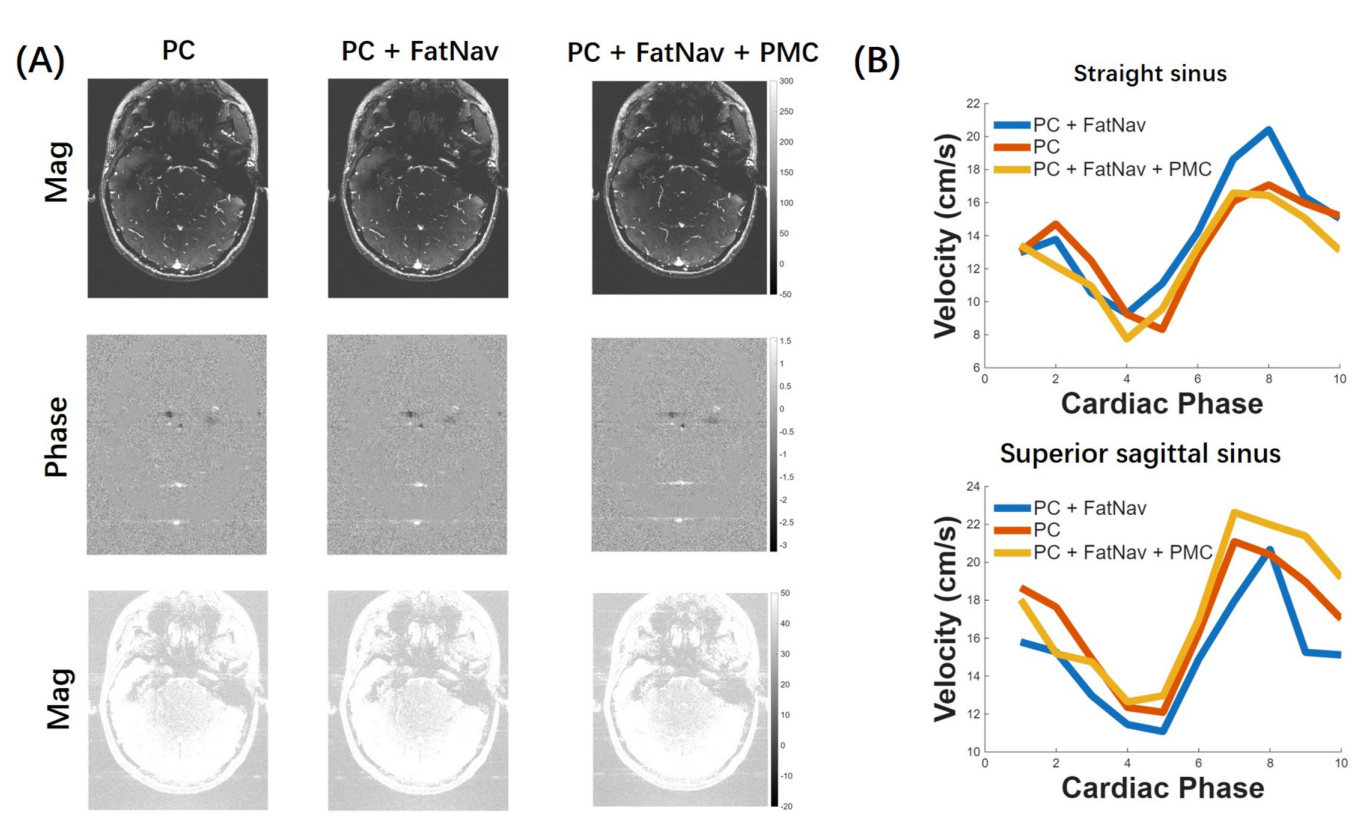


FIGURE 6 | (A) PC-MRI images acquired without FatNav or PMC, with FatNav but no PMC, and with FatNav and PMC, respectively, when the head remained still. Top two rows show representative magnitude and phase images. Third row shows magnitude images with adjusted intensity window to highlight ghosting artifacts in the background. (B) Blood flow velocity waveforms in the straight and superior sagittal sinus under the three FatNav and PMC settings.

(SSS/SRS) between FatNav off and FatNav on but PMC off, and 0.9997 ± 0.0002 (CAq) and 0.9984 ± 0.0007 (SSS/SRS) for FatNav off versus PMC on.

CSF and blood flow velocity waveforms over the cardiac cycle were extracted from all three acquisition types. The resulting waveforms showed high consistency, as shown in Figures 5B and 6B, with average correlation coefficients of 0.997/0.769/0.606 (FatNav off vs. FatNav on but PMC off) and 0.973/0.666/0.511 (FatNav off vs. PMC on) for the CAq, SSS, and SRS, respectively. There was no significant difference between the three conditions in any parameters, as shown in Figure 7A–F, suggesting that the FatNav and PMC modules did not adversely affect image quality or flow quantification.

Figures 8 and 9 show representative PC-MRI images acquired under still, motion with PMC on and motion with PMC off conditions, respectively. The corresponding motion traces are shown in Figures 8S-11S, where the head motion ranges were similar between the PMC-on and PMC-off conditions. Compared to PMC off, the PC MRI images with PMC on exhibited higher boundary clarity of the CAq, resembling more closely to the still images.

As illustrated in Figure 10A–F, the mean deviations of $F_{\rm abs}$ and $V_{\rm range}$ of CAq in the PMC on condition from the still scans were $-0.42\pm2.43\,{\rm mL/min}\,(p\!=\!0.36)$ and $0.59\pm1.34\,{\rm cm/s}\,(p\!=\!0.0501)$, respectively, whereas the deviations in the PMC off condition were $1.68\pm2.46\,{\rm mL/min}\,(p\!=\!3.2^*10^{-4})$ and $2.00\pm2.33\,{\rm cm/s}$

 $(p=2.1*10^{-4})$. The mean deviations of $F_{\rm abs}$ and mean velocity in the PMC on condition from the still scans were $16.7\pm42.7\,{\rm mL/min}$ (SSS) and $-4.7\pm27.0\,{\rm mL/min}$ (SRS) and $0.66\pm1.68\,{\rm cm/s}$ (SSS) and $0.93\pm2.84\,{\rm cm/s}$ (SRS), respectively, whereas the deviations in the PMC off condition were $40.98\pm40.69\,{\rm mL/min}$ ($p=5.9*10^{-4}$) (SSS) / $17.8\pm26.3\,{\rm mL/min}$ (p=0.006) (SRS) and $0.79\pm1.37\,{\rm cm/s}$ (p=0.029) (SSS) / $1.12\pm2.71\,{\rm cm/s}$ (p=0.048) (SRS). The results between still and PMC off conditions were significantly different. However, there was no clear linear correlation between the motion score and the relative changes in the measured parameters, as shown in Figure 12S.

3.2 | Posture Dependence

One SSS/SRS image pairs (supine vs. prone) were excluded because of the presence of severe motion artifacts. Furthermore, IJV and SRS could not be identified in four and two subjects, respectively, resulting in 14 sets of heart rate data, 14 CAq datasets, 14 ICA datasets, 14 VA datasets, 10 IJV datasets, 13 SSS datasets, and 11 SRS datasets for analysis.

3.2.1 | Consistent Slice Prescription

Figure 11 presents representative magnitude images from different regions in the supine and prone postures, both of which exhibited high similarity, with SSIM values of 0.9913 ± 0.004 , 0.9930 ± 0.002 , and 0.9875 ± 0.004 for the CAq, VA/ICA/IJV,

NMR in Biomedicine, 2025 9 of 18

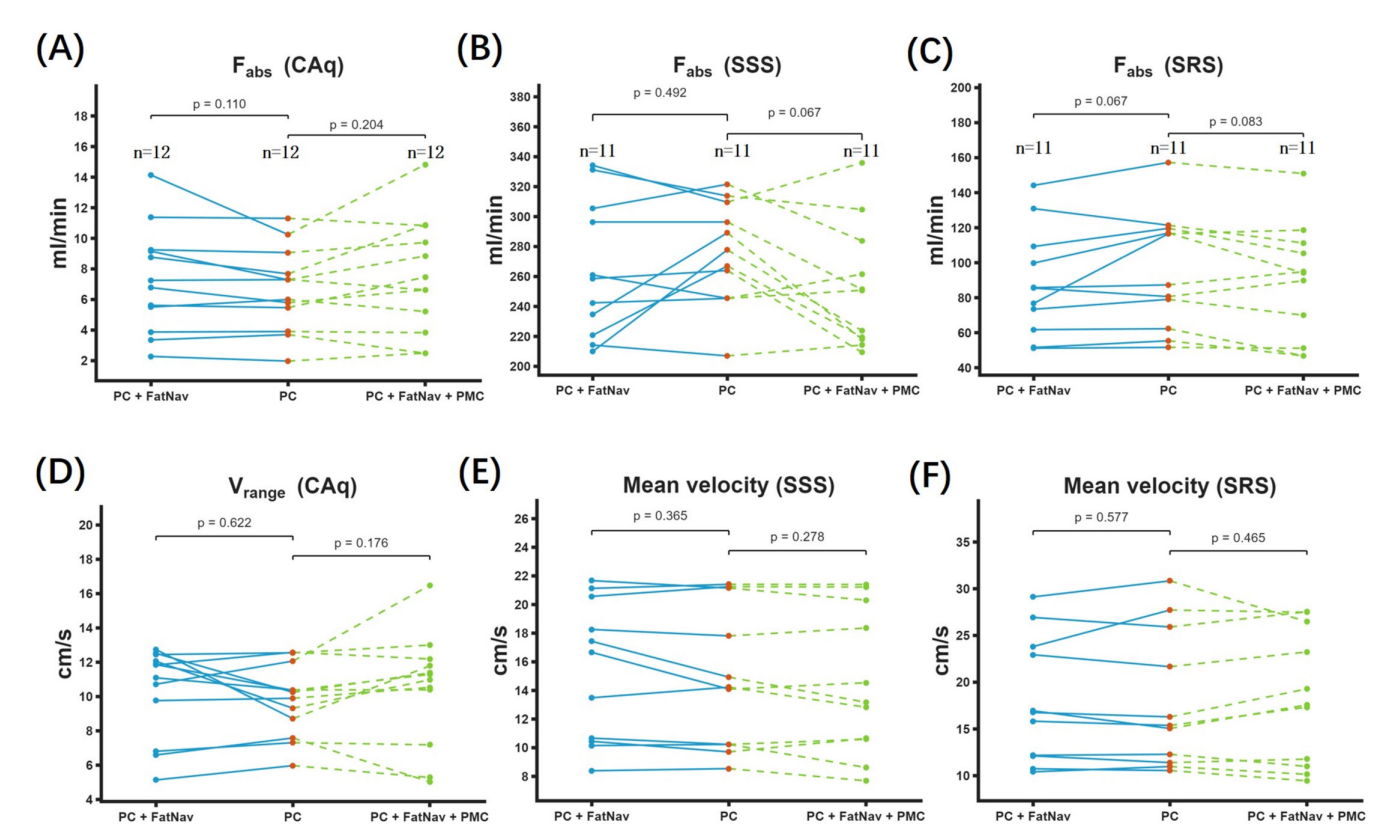


FIGURE 7 | (A–C) show the changes in F_{abs} in the CAq, SSS, and SRS under three conditions (PC, PC with FatNav, and PC with FatNav and PMC) during head-still scans. (D–F) show the corresponding changes in V_{range} or mean velocity in Caq, SSS and SRS under the same conditions.

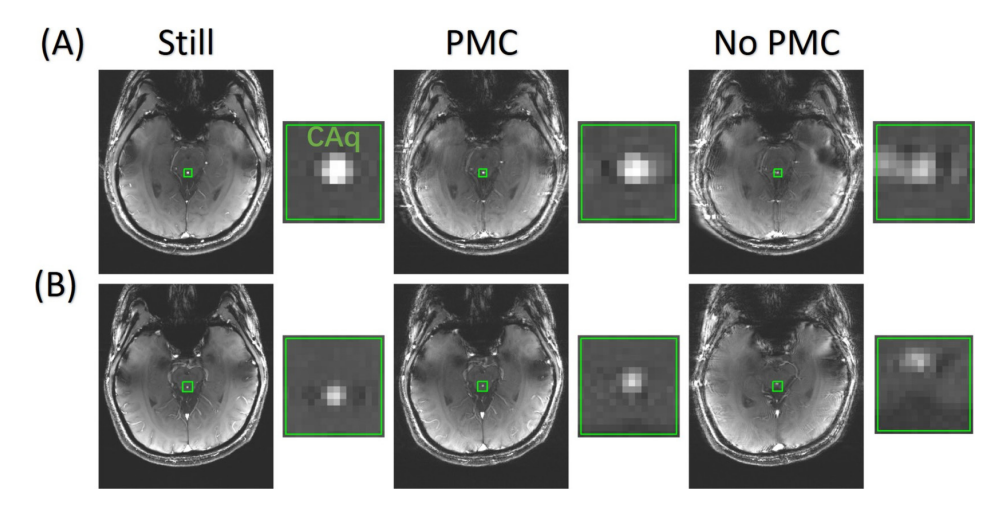


FIGURE 8 | Representative PC-MRI images acquired under three conditions: still, head motion with PMC, and head motion without PMC in two subjects. Green boxes indicate the boundary of the enlarged views displayed adjacent to each image to highlight the CAq at the center.

and SSS/SRS images, respectively. It should be noted that, because blood flow parameters naturally differ between supine and prone postures, their repeatability was not assessed.

3.2.2 | Heart Rate

Heart rate increased when participants changed from the supine to the prone posture. The mean heart rates in the supine and prone postures were 68 ± 5 and 75 ± 7 bpm, respectively. The relative increase was $10\% \pm 9\%$, which was statistically significant (p = 0.0001).

3.2.3 | CSF and Blood Flow

Figure 12A–E compares $F_{\rm abs}$, stroke volume, area, mean velocity, and $V_{\rm range}$ of different vessels under supine and prone postures. The mean and standard deviation of each parameter are listed in Table 3. Figure 13A–F illustrates the dynamic changes in flow velocity within the vessels throughout the cardiac cycle.

No significant difference in mean velocity or area was observed in any vessels between the supine and prone postures ($p \ge 0.33$). However, stroke volume, absolute flow, and $V_{\rm range}$ decreased significantly in CAq in the prone posture. Stroke

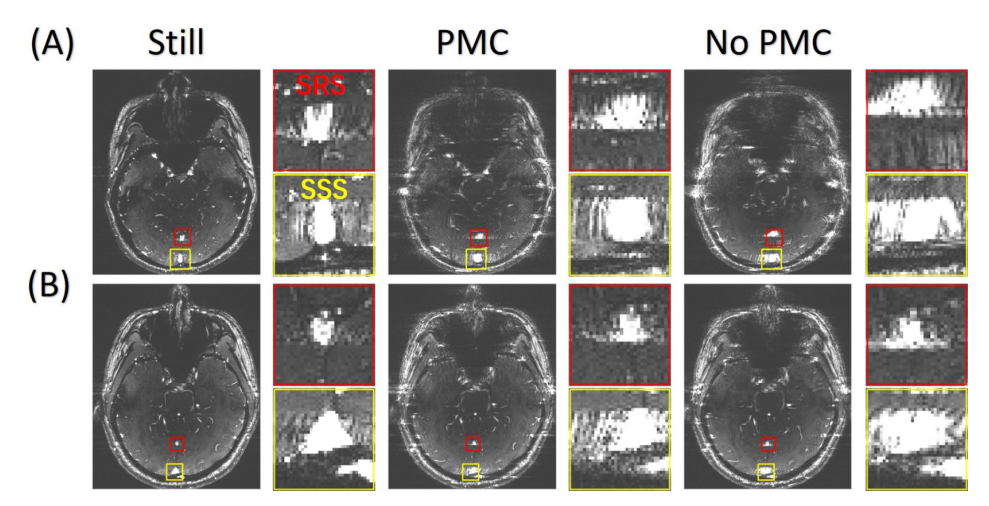


FIGURE 9 | Representative PC-MRI images acquired under three conditions: still, head motion with PMC, and head motion without PMC. Red boxes indicate the regions containing the SRS, and yellow boxes indicate the regions containing the SSS. Enlarged views of these regions are displayed adjacent to each image to highlight the vessels at the center.

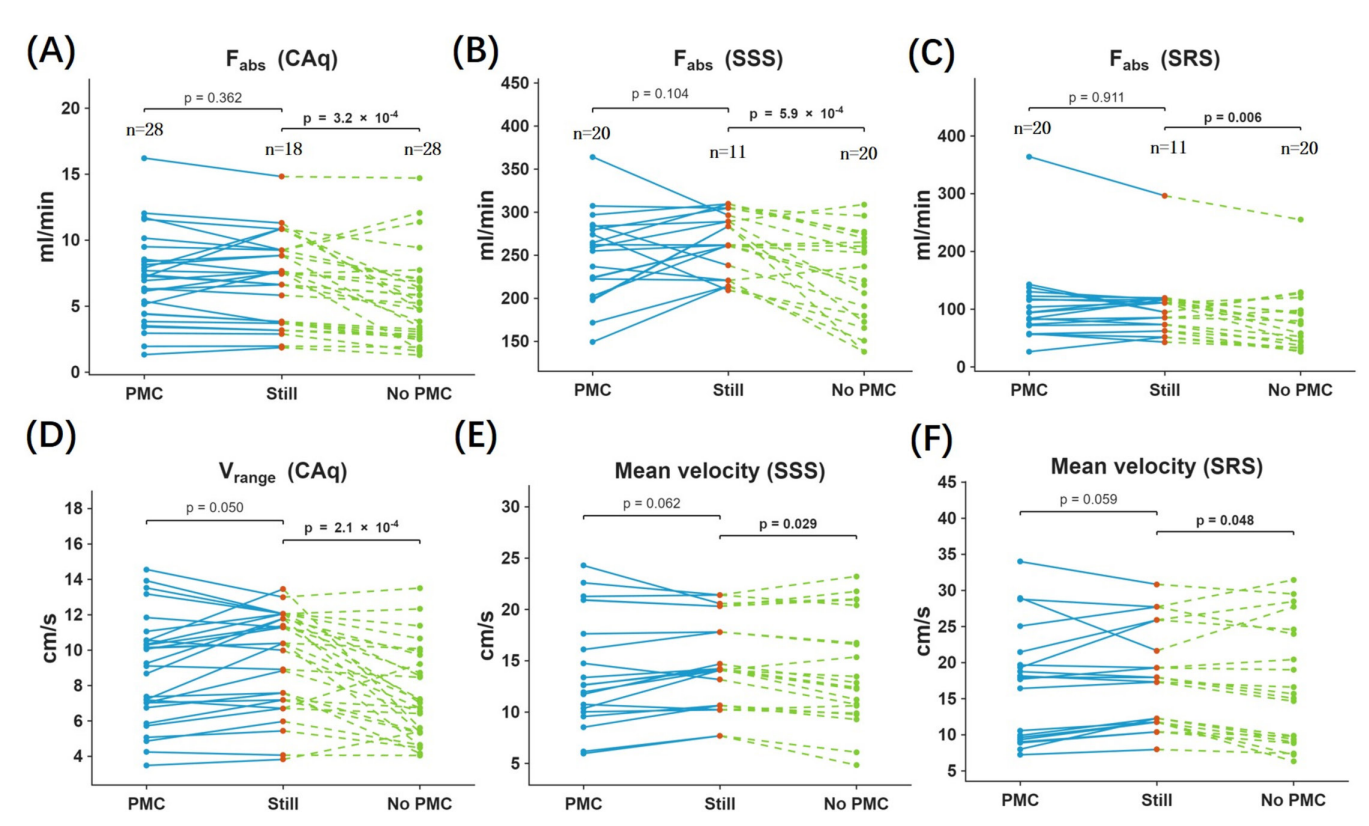


FIGURE 10 | (A–C) show F_{abs} in the CAq, SSS, and SRS under still and PMC and No-PMC conditions during controlled head motion. (D–F) show V_{range} , or blood flow mean velocity in Caq, SSS, and SRS under the same conditions.

volume also decreased significantly in ICA and IJV in the prone posture.

3.2.4 | Correlation Between CSF and Blood Flow Changes

Significant positive correlations were observed between posture-induced stroke volume changes in the ICA and those in IJV and CAq, with Spearman correlation coefficients of

0.76 (p=0.016) and 0.55 (p=0.044), respectively, as shown in Figure 12F–H. To evaluate the coupling between cardiac phase dependent CSF and blood flow dynamics, scatter plots of CSF and blood flow velocities at different cardiac phases were obtained. A strong negative correlation was obtained under both supine and prone postures, with Spearman correlation coefficients of ρ =-0.96 (p=10⁻⁵⁰) and ρ =-0.84 (p=0.004), respectively, as shown in Figure 13G. Note that to account for potential delay of CAq flow velocity changes relative to the arterial blood, the curve for CAq was shifted leftward by one time point (1/10

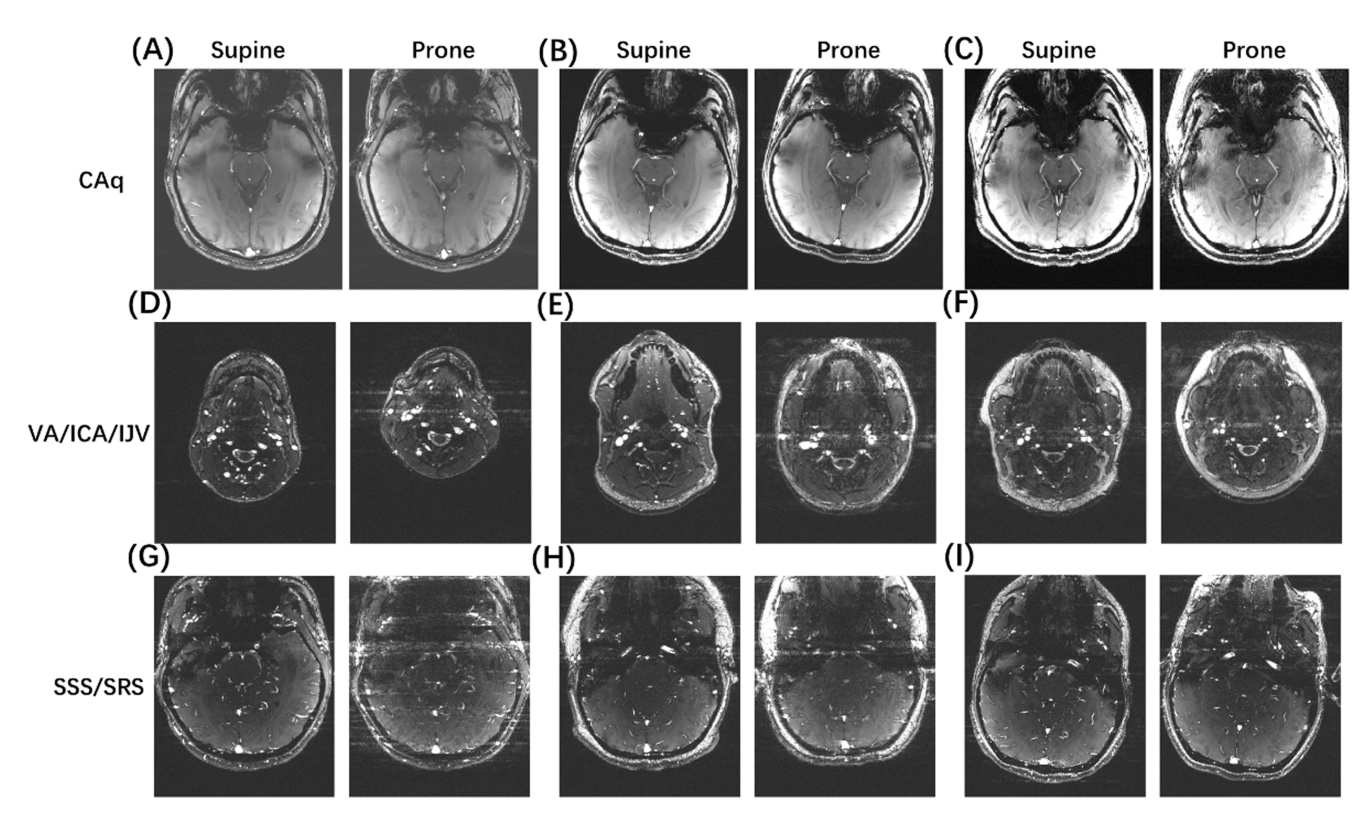


FIGURE 11 | Comparison of magnitude images from different regions acquired in the supine and prone postures in three representative subjects.

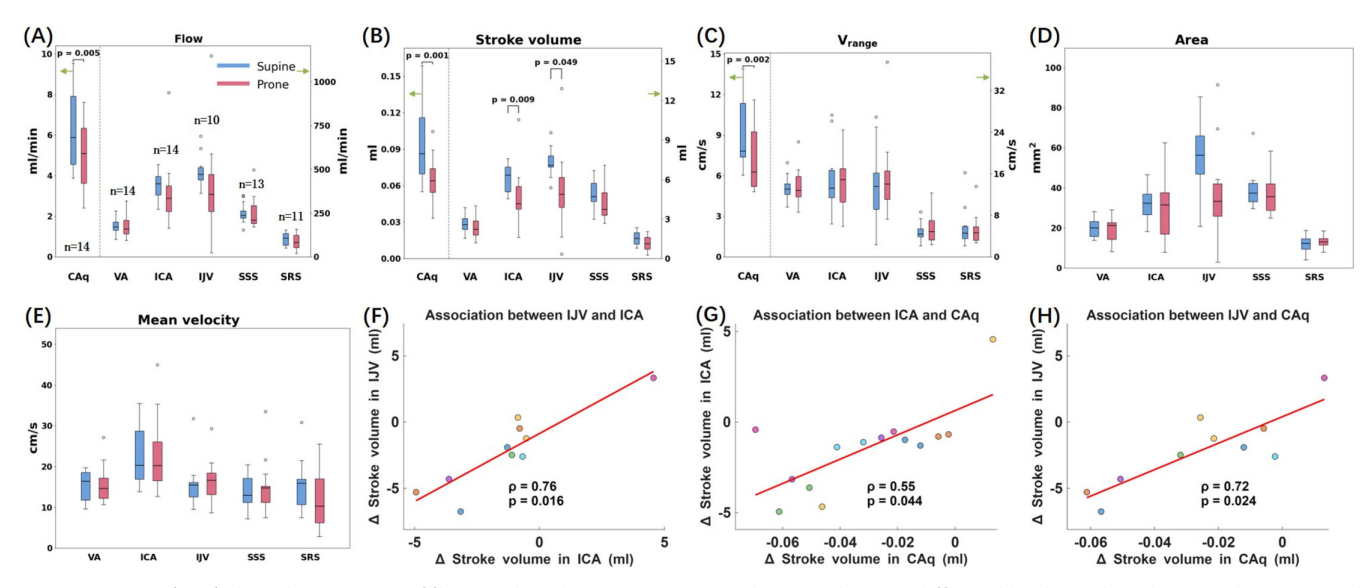


FIGURE 12 | (A-F) show the variations of flow, stroke volume, V_{range} , area, and mean velocity in different blood vessels and CAq under supine and prone postures. Data to the left of the dashed line correspond to the left y-axis, while data to the right correspond to the right y-axis. (F-H) show the scatter plots between posture-induced stroke volume changes in ICA and IJV, ICA and CAq, and CAq and IJV, respectively. Each color represents a different subject. The straight lines are best linear fits.

cardiac cycle). It has been reported that the peak caudal flow of CSF lags behind the peak flow in the ICA by approximately 60 ms, which roughly corresponds to 1/10 cardiac cycle [50].

4 | Discussion

To simultaneously investigate the differences in CSF and blood flow between the supine and prone postures, as well as their coupling relationships, this study developed an automatic localization and PMC framework for vessel fluid measurements and applied the developed methods to measure the dynamic changes of CSF and blood flow during the supine and prone postures. The main findings are summarized as follows: (1) 3D U-Net based CAq segmentation allows automatic prescription of PC-MRI slice for measuring CSF flow dynamics across CAq. (2) Slice position transformation based on registration of 3D images allows consistent imaging of the

TABLE 3 | Mean and standard deviation of F_{abs} , stroke volume, V_{range} , area, and mean velocity for the CAq and blood vessels. Bold values indicate statistically significant differences (p < 0.05).

		Stroke volume (mL)		Area (mm²)		F _{abs} (mL/min)		V _{range} (cm/s)		Mean velocity (cm/s)		
	Posture	Mean (SD)	p	Mean (SD)	p	Mean (SD)	p	Mean (SD)	p	Mean (SD)	p	n
CAq	Supine	0.09 (0.03)	0.001	3.9 (1.4)	1	6.3 (1.9)	0.005	9.2 (2.5)	0.002	N/A	N/A	14
	Prone	0.06 (0.02)		3.9 (1.4)		5.0 (1.5)		7.2 (2.2)		N/A		
VA	Supine	2.6 (0.7)	0.09	20 (5)	0.76	177 (45)	0.90	13.1 (2.3)	0.76	15 (4)	0.83	14
	Prone	2.3 (1.0)		20 (5)		177 (61)		13.5 (3.4)		16 (4)		
ICA	Supine	6.1 (1.0)	0.009	32 (8)	0.33	407 (72)	0.12	14.8 (5.7)	0.81	23 (7)	0.83	14
	Prone	4.7 (2.0)		30 (15)		365 (184)		14.6 (5.0)		23 (9)		
IJV	Supine	7.3 (1.1)	0.048	57 (19)	0.33	491 (94)	0.23	13.7 (7.5)	0.49	16 (6)	0.83	10
	Prone	5.2 (3.2)		39 (24)		403 (294)		15.7 (8.1)		17 (5)		
SSS	Supine	4.8 (1.0)	0.18	39 (9)	0.33	248 (55)	0.74	4.9 (1.7)	0.27	14 (4)	0.83	13
	Prone	4.1 (1.2)		37 (9)		254 (88)		5.5 (2.9)		15 (6)		
SRS	Supine	1.5 (1.1)	0.07	11 (4)	0.33	100 (37)	0.64	5.7 (3.8)	0.97	15 (6)	0.83	11
	Prone	1.1 (0.6)		12 (3)		86 (45)		5.3 (3.0)		11 (7)		

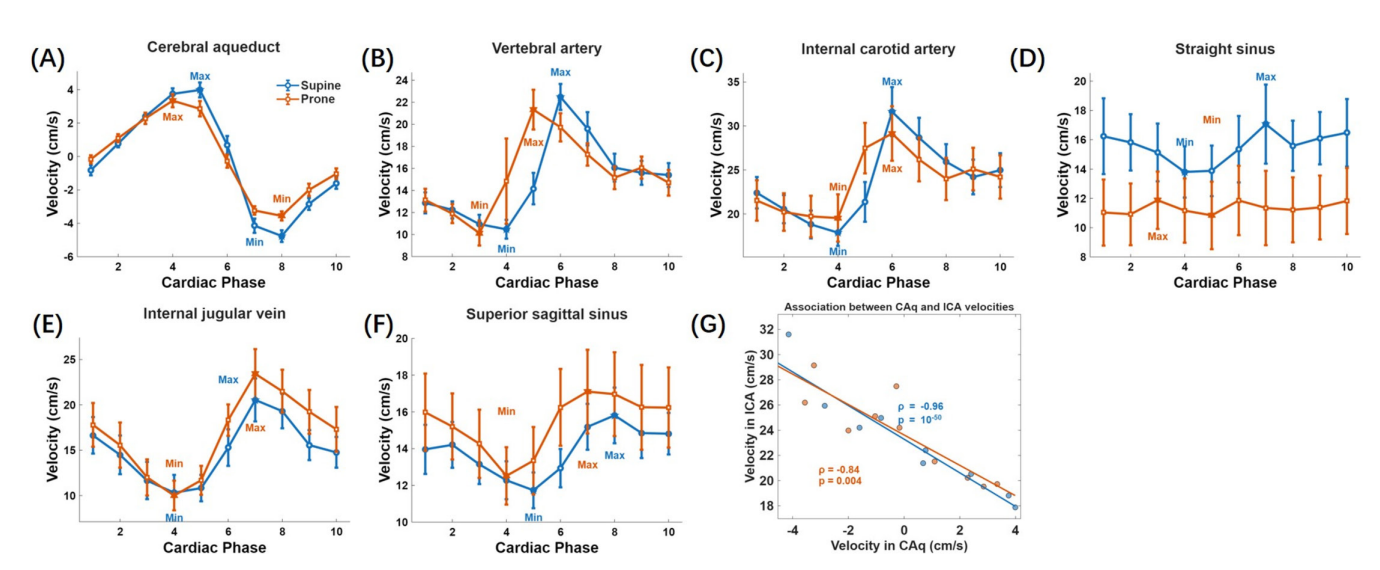


FIGURE 13 | (A–F) Group averaged flow velocity curves across different cardiac phases for the CAq, VA, ICA, IJV, SSS, and SRS, respectively. The labelled positions of the maximum and minimum values on the curves were used to calculate the V_{range} for each subject. In Figures (A–C) and (D–F), positive values correspond to flow toward the head and feet, respectively. (G) shows the scatter plots of the ICA and CAq velocities. Different data points represent different cardiac phases. The CAq time course was shifted leftward by one time point before used for making the scatter plot.

same brain location in longitudinal studies. (3) FatNav based motion correction for PC-MRI is feasible at 3T and significantly increases image quality and the accuracy of velocity measurement. (4) Compared to the supine posture, absolute flows of CAq, ICA, and IJV significantly decrease in the prone posture. (5) Posture-dependent changes in ICA, IJV, and CAq stroke volumes were positively correlated.

4.1 | Technical Development

4.1.1 | CAq Segmentation and Slice Prescription

The aqueduct mask obtained by 3D U-Net segmentation was highly consistent with the manually defined aqueduct mask in terms of both position and orientation of the calculated scan

plane. This finding indicates that the localization method based on automatically segmented CAq masks eliminates operator dependency. In addition, it improves the consistency and efficiency of scan prescription.

4.1.2 | Consistent Slice Prescription

By applying image registration, the same anatomical location can be consistently prescribed across different scans. This approach reduces operator-dependent variability arising from manual adjustments and ensures consistent slice positioning across different time points or postural conditions, providing a reliable basis for subsequent quantitative analyses.

The images acquired after repositioning were highly similar to the initial images, as indicated by the high SSIM values. Furthermore, the repeatability of flow parameters measured after repositioning was even smaller than that obtained from continuous scans without repositioning. The results indicate that the slice prescription based on registration can ensure consistent flow measurement results. Such consistency is particularly important for longitudinal studies, as it ensures that flow measurements obtained at different time points are comparable, thereby enhancing the reliability of follow-up investigations.

Moreover, our results showed that a deviation of approximately 6° between the imaging plane and the aqueduct axis did not produce significant differences in flow parameters. Such robustness is practically important, as achieving perfect orthogonality between the imaging plane and the flow direction is often difficult in clinical and research settings.

4.1.3 | FatNav-Based PMC

Our study demonstrates that FatNav-based PMC is also feasible at 3T, despite smaller frequency separation between water and fat protons, as the inclusion of the FatNav and PMC modules into the PC-MRI sequence did not affect image quality and flow parameters. PMC effectively reduces motion-related artifacts, enhances the clarity of vascular structures, and improves the accuracy of flow dynamics quantification, all without increasing scan time and without the need for additional equipment. PMC is particularly relevant to clinical studies, as subject motion or positional changes during MRI acquisition can introduce motion artifacts and variability in quantitative results, particularly in elderly or pediatric populations where involuntary movements are more common [51-53]. The lack of correlation between motion score and the relative changes of flow parameters may be explained by the dependence of motion effects on motion patterns, which is not incorporated into the motion score calculation.

4.2 | Posture Effects

We observed a reduction in stroke volume in ICA but no change in blood flow, when switching from the supine to prone posture, consistent with previous studies [21–26]. The

stroke volume reduction was likely due to decreased stroke volume from the lower body, as a result of thoracic compression [54–61]. Interestingly, the VA did not show significant changes. This may be related to the protection of VA by surrounding bony structures, which results in less variable flow in VA than ICA [62]. In addition, prone posture can stimulate sympathetic neural activity [57], resulting in elevated heart rate which compensate the stroke volume reduction and lead to stable cerebral perfusion. Although heart rate increased, the mechanical contraction of the heart remains physiologically stable [63]. Therefore, flow, mean velocity, and $V_{\rm range}$ in the blood vessels may not change significantly.

We found that, compared with the supine posture, the prone posture was associated with reduced CSF stroke volume and absolute flow rate. We suspect that the reduction in arterial stroke volume may lead to increased sympathetic tone, which in turn could elevate adrenaline secretion [58, 64, 65] and reduce CSF flow and stroke volume [10, 20, 56, 66], thereby impairing the clearance of brain waste products [56, 67]. Furthermore, we observed a significant negative correlation between the cardiac-phase-dependent flow velocity of the ICA and that of the CSF. This finding is consistent with previous reports of spatiotemporal coupling between blood and CSF dynamics in the human brain [68], suggesting that arterial pulsation plays a key role in driving CSF circulation [58]. Therefore, the reduction in ICA stroke volume may also lead to reduced driving force for CSF circulation, resulting in reduced stroke volume across CAq. Animal experimental studies have suggested that CSF circulation and convective exchange are closely linked to metabolic waste clearance [29]. Thus, a sustained reduction in CSF stroke volume may plausibly impair glymphatic transport. However, direct evidence for this mechanism in humans is still lacking and warrants further investigation.

Changes in posture and head position (e.g., head rotation) can affect the area of cervical vessels [60]. Previous studies have reported that these vessels typically show an increased area in the prone posture [21, 22]. However, in the present study, this change did not reach statistical significance. We speculate that two factors may account for this discrepancy. First, the participants remained in the prone posture for only a short period, which might be insufficient for the slower adaptation of vessel area to occur [22]. Second, it was difficult for participants to maintain a completely neutral head position in the prone posture. In fact, five subjects exhibited varying degrees of head rotation. Previous studies have shown that head rotation can reduce the area of cervical vessels [60, 69]. On the other hand, the lack of changes in cross-sectional areas of SSS and SRS may be explained by their coverage by the thick dura mater.

4.3 | Limitations

Our study has the following limitations.

First, the segmentation model in this study was trained only on healthy subjects. Since aqueduct morphology may vary substantially in patients (e.g., in hydrocephalus), the current model may not generalize directly to pathological populations. Future work

should incorporate representative patient data into the training process and validate the method in clinical cohorts.

Second, in this study, the segmentation-based automatic slice prescription was applied only to the CAq. Such an approach could also be developed for the imaging slices targeting other vessels. However, as multiple vessels are simultaneously measured in the other slices, the determination of slice position should consider the possibility of nonparallelism between the vessels.

Third, although our automatic localization method demonstrated high efficiency and accuracy, it relies on the acquisition and processing of T2WI, which requires several minutes. During this time, subjects may undergo head movements, leading to suboptimal slice positioning. In the future, implementing FatNav-based PMC in the T2WI scan and registering all subsequent FatNav images from the PC scans to the first FatNav from the T2WI scan can eliminate the slice shift due to inter-scan motion.

Fourth, our PMC method is designed for rigid structures, and its effectiveness remains limited when applied to nonrigid structures such as cervical vessels.

Fifth, due to the limited space inside the RF coils, we were unable to investigate CSF and CBF dynamics in lateral decubitus positions.

Sixth, the cardiac cycle was divided into only 10 phases, which is likely insufficient to capture subtle details of the dynamic velocity curves. However, the study is mainly focused on the total flow measurement whose accuracy is likely insensitive to the number of cardiac phases.

5 | Conclusions

In conclusion, we demonstrated the utility of PMC and automatic slice prescription in facilitating 2D PC-MRI in longitudinal studies. With the developed techniques, we found significant postural effects in flow properties in CAq, ICA, and IJV. Furthermore, cardiac phase-dependent variations in flow velocity and posture-induced changes in stroke volume were correlated between CAq and blood vessels. The findings overall suggest the important role of arterial pulsation in regulating CSF circulation, which might be reduced in prone posture compared to supine.

Author Contributions

Tuo Yu: methodology, data collection, technical implementation, data analysis, and manuscript writing; Shaonong Wei: image segmentation; Jiayu Zhu and Xin Ye: technical support; Xiaopeng Zong: conceptualization, supervision, manuscript revision, and correspondence.

Conflicts of Interest

The authors declare no conflicts of interest.

Data Availability Statement

The data that support the findings of this study are openly available in YuTuoData at https://doi.org/10.5281/zenodo.17055176 and https://pan.baidu.com/s/11bOrvn0eu0D2fcMt_0axIA (access code: 3agu).

References

- 1. A. Ruitenberg, T. den Heijer, S. L. Bakker, et al., "Cerebral Hypoperfusion and Clinical Onset of Dementia: The Rotterdam Study," *Annals of Neurology* 57, no. 6 (2005): 789–794, https://doi.org/10.1002/ana.20493.
- 2. H. Whitley, P. Skalický, A. Zazay, A. Bubeníková, and O. Bradáč, "Volumes and Velocities: Meta-Analysis of PC-MRI Studies in Normal Pressure Hydrocephalus," *Acta Neurochirurgica* 166, no. 1 (2024): 463, https://doi.org/10.1007/s00701-024-06333-2.
- 3. S. W. Bothwell, D. Janigro, and A. Patabendige, "Cerebrospinal Fluid Dynamics and Intracranial Pressure Elevation in Neurological Diseases," *Fluids and Barriers of the CNS* 16, no. 1 (2019): 9, https://doi.org/10.1186/s12987-019-0129-6.
- 4. J. M. Kollmeier, L. Gürbüz-Reiss, P. Sahoo, et al., "Deep Breathing Couples CSF and Venous Flow Dynamics," *Scientific Reports* 12, no. 1 (2022): 2568, https://doi.org/10.1038/s41598-022-06361-x.
- 5. V. Vinje, G. Ringstad, E. K. Lindstrøm, et al., "Respiratory Influence on Cerebrospinal Fluid Flow A Computational Study Based on Long-Term Intracranial Pressure Measurements," *Scientific Reports* 9, no. 1 (2019): 9732, https://doi.org/10.1038/s41598-019-46055-5.
- 6. S. Yildiz, S. Thyagaraj, N. Jin, et al., "Quantifying the Influence of Respiration and Cardiac Pulsations on Cerebrospinal Fluid Dynamics Using Real-Time Phase-Contrast MRI," *Journal of Magnetic Resonance Imaging* 46, no. 2 (2017): 431–439, https://doi.org/10.1002/jmri.25591.
- 7. G. Baselli, F. Fasani, L. Pelizzari, M. Cazzoli, F. Baglio, and M. M. Laganà, "Real-Time Phase-Contrast MRI to Monitor Cervical Blood and Cerebrospinal Fluid Flow Beat-by-Beat Variability," *Biosensors* 12, no. 6 (2022): 417, https://doi.org/10.3390/bios12060417.
- 8. M. M. Laganà, S. Di Tella, F. Ferrari, et al., "Blood and Cerebrospinal Fluid Flow Oscillations Measured With Real-Time Phase-Contrast MRI: Breathing Mode Matters," *Fluids and Barriers of the CNS* 19, no. 1 (2022): 100, https://doi.org/10.1186/s12987-022-00394-0.
- 9. J. Daouk, R. Bouzerar, and O. Baledent, "Heart Rate and Respiration Influence on Macroscopic Blood and CSF Flows," *Acta Radiologica* 58, no. 8 (2017): 977–982, https://doi.org/10.1177/0284185116676655.
- 10. H. Mestre, J. Tithof, T. Du, et al., "Flow of Cerebrospinal Fluid is Driven by Arterial Pulsations and Is Reduced in Hypertension," *Nature Communications* 9, no. 1 (2018): 4878, https://doi.org/10.1038/s41467-018-07318-3.
- 11. R. A. Bhadelia, A. R. Bogdan, and S. M. Wolpert, "Cerebrospinal Fluid Flow Waveforms: Effect of Altered Cranial Venous Outflow. A Phase-Contrast MR Flow Imaging Study," *Neuroradiology* 40, no. 5 (1998): 283–292, https://doi.org/10.1007/s002340050586.
- 12. S. D. Williams, B. Setzer, N. E. Fultz, et al., "Neural Activity Induced by Sensory Stimulation Can Drive Large-Scale Cerebrospinal Fluid Flow During Wakefulness in Humans," *PLoS Biology* 21, no. 3 (2023): e3002035, https://doi.org/10.1371/journal.pbio.3002035.
- 13. T. Tarumi, T. Yamabe, M. Fukuie, et al., "Brain Blood and Cerebrospinal Fluid Flow Dynamics During Rhythmic Handgrip Exercise in Young Healthy Men and Women," *Journal of Physiology* 599, no. 6 (2021): 1799–1813, https://doi.org/10.1113/jp281063.
- 14. A. F. Sagirov, T. V. Sergeev, A. V. Shabrov, A. Y. Yurov, N. L. Guseva, and E. A. Agapova, "Postural Influence on Intracranial Fluid Dynamics: An Overview," *Journal of Physiological Anthropology* 42, no. 1 (2023): 5, https://doi.org/10.1186/s40101-023-00323-6.

- 15. M. Matsumae, T. Murakami, M. Ueda, Y. Suzuki, and O. Sato, "Dynamic Changes of Cerebrospinal Fluid Shunt Flow in Patient's Daily Life," *Child's Nervous System* 3, no. 1 (1987): 30–34, https://doi.org/10.1007/bf00707190.
- 16. M. Hidaka, M. Matsumae, K. Ito, R. Tsugane, and Y. Suzuki, "Dynamic Measurement of the Flow Rate in Cerebrospinal Fluid Shunts in Hydrocephalic Patients," *European Journal of Nuclear Medicine* 28, no. 7 (2001): 888–893, https://doi.org/10.1007/s002590100547.
- 17. N. Alperin, S. G. Hushek, S. H. Lee, A. Sivaramakrishnan, and T. Lichtor, "MRI Study of Cerebral Blood Flow and CSF Flow Dynamics in an Upright Posture: The Effect of Posture on the Intracranial Compliance and Pressure," in *Acta Neurochir Suppl*, vol. 95, (Springer-Verlag, 2005), 177–181, https://doi.org/10.1007/3-211-32318-x 38.
- 18. N. Alperin, S. H. Lee, and A. M. Bagci, "MRI Measurements of Intracranial Pressure in the Upright Posture: The Effect of the Hydrostatic Pressure Gradient," *Journal of Magnetic Resonance Imaging* 42, no. 4 (2015): 1158–1163, https://doi.org/10.1002/jmri.24882.
- 19. N. Watanabe, J. Reece, and B. I. Polus, "Effects of Body Position on Autonomic Regulation of Cardiovascular Function in Young, Healthy Adults," *Chiropractic & Osteopathy* Nov 28, 15 (2007): 19, https://doi.org/10.1186/1746-1340-15-19.
- 20. M. Muccio, D. Chu, L. Minkoff, et al., "Upright Versus Supine MRI: Effects of Body Position on Craniocervical CSF Flow," *Fluids and Barriers of the CNS* 18, no. 1 (2021): 61, https://doi.org/10.1186/s12987-021-00296-7
- 21. T. Y. Yeoh, A. Tan, P. Manninen, V. W. Chan, and L. Venkatraghavan, "Effect of Different Surgical Positions on the Cerebral Venous Drainage: A Pilot Study Using Healthy Volunteers," *Anaesthesia* 71, no. 7 (2016): 806–813, https://doi.org/10.1111/anae.13494.
- 22. D. Montero and S. Rauber, "Brain Perfusion and Arterial Blood Flow Velocity During Prolonged Body Tilting," *Aerospace Medicine and Human Performance* 87, no. 8 (2016): 682–687, https://doi.org/10.3357/amhp.4546.2016.
- 23. Y. Taj, N. Samagh, S. U. Paliwal, V. Ganesh, A. Dey, and V. Aggarwal, "Effect of Prone Position on Cerebral Hemodynamics and Noninvasive Intracranial Pressure Assessed Using Transcranial Doppler in Patients Undergoing Spine Surgeries: A Prospective Observational Study," *BMC Anesthesiology* 25, no. 1 (2025): 242, https://doi.org/10.1186/s12871-025-03116-9.
- 24. T. Kato, T. Kurazumi, T. Konishi, C. Takko, Y. Ogawa, and K. I. Iwasaki, "Effects of -10° and -30° Head-Down Tilt on Cerebral Blood Velocity, Dynamic Cerebral Autoregulation, and Noninvasively Estimated Intracranial Pressure," *Journal of Applied Physiology (Bethesda, MD: 1985)* 132, no. 4 (2022): 938–946, https://doi.org/10.1152/japplphysiol.00283.2021.
- 25. J. C. Geinas, K. R. Marsden, Y. C. Tzeng, et al., "Influence of Posture on the Regulation of Cerebral Perfusion," *Aviation, Space, and Environmental Medicine* 83, no. 8 (2012): 751–757, https://doi.org/10.3357/asem. 3269.2012.
- 26. E. L. Vu, C. H. Brown, K. M. Brady, and C. W. Hogue, "Monitoring of Cerebral Blood Flow Autoregulation: Physiologic Basis, Measurement, and Clinical Implications," *British Journal of Anaesthesia* 132, no. 6 (2024): 1260–1273, https://doi.org/10.1016/j.bja.2024.01.043.
- 27. C. Guérin, J. Reignier, J.-C. Richard, et al., "Prone Positioning in Severe Acute Respiratory Distress Syndrome," *New England Journal of Medicine* 368, no. 23 (2013): 2159–2168, https://doi.org/10.1056/NEJMo a1214103.
- 28. N. E. Fultz, G. Bonmassar, K. Setsompop, et al., "Coupled Electrophysiological, Hemodynamic, and Cerebrospinal Fluid Oscillations in Human Sleep," *Science* 366, no. 6465 (2019): 628–631, https://doi.org/10.1126/science.aax5440.

- 29. L. Xie, H. Kang, Q. Xu, et al., "Sleep Drives Metabolite Clearance From the Adult Brain," *Science* 342, no. 6156 (2013): 373–377, https://doi.org/10.1126/science.1241224.
- 30. D. T. Wymer, K. P. Patel, W. F. Burke, and V. K. Bhatia, "Phase-Contrast MRI: Physics, Techniques, and Clinical Applications," *Radiographics* 40, no. 1 (2020): 122–140, https://doi.org/10.1148/rg.20201 90039.
- 31. D. R. Enzmann and N. J. Pelc, "Normal Flow Patterns of Intracranial and Spinal Cerebrospinal Fluid Defined With Phase-Contrast Cine MR Imaging," *Radiology* 178, no. 2 (1991): 467–474, https://doi.org/10.1148/radiology.178.2.1987610.
- 32. D. Greitz, A. Franck, and B. Nordell, "On the Pulsatile Nature of Intracranial and Spinal CSF-Circulation Demonstrated by MR Imaging," *Acta Radiologica* 34, no. 4 (1993): 321–328.
- 33. G. Schroth and U. Klose, "MRI of CSF Flow in Normal Pressure Hydrocephalus," *Psychiatry Research* 29, no. 3 (1989): 289–290, https://doi.org/10.1016/0165-1781(89)90066-8.
- 34. G. Pagé, J. Bettoni, A. V. Salsac, and O. Balédent, "Influence of Principal Component Analysis Acceleration Factor on Velocity Measurement in 2D and 4D PC-MRI," *Magnetic Resonance Materials in Physics, Biology and Medicine* 31, no. 3 (2018): 469–481, https://doi.org/10.1007/s10334-018-0673-0.
- 35. A. F. Stalder, M. F. Russe, A. Frydrychowicz, J. Bock, J. Hennig, and M. Markl, "Quantitative 2D and 3D Phase Contrast MRI: Optimized Analysis of Blood Flow and Vessel Wall Parameters," *Magnetic Resonance in Medicine* 60, no. 5 (2008): 1218–1231, https://doi.org/10.1002/mrm.21778.
- 36. J. Maclaren, M. Herbst, O. Speck, and M. Zaitsev, "Prospective Motion Correction in Brain Imaging: A Review," *Magnetic Resonance in Medicine* 69, no. 3 (2013): 621–636, https://doi.org/10.1002/mrm. 24314.
- 37. A. Schulz, D. F. A. Lloyd, M. P. M. van Poppel, et al., "Structured Analysis of the Impact of Fetal Motion on Phase-Contrast MRI Flow Measurements With Metric Optimized Gating," *Scientific Reports* 12, no. 1 (2022): 5395, https://doi.org/10.1038/s41598-022-09327-1.
- 38. H. Olsson, J. M. Millward, L. Starke, et al., "Simulating Rigid Head Motion Artifacts on Brain Magnitude MRI Data-Outcome on Image Quality and Segmentation of the Cerebral Cortex," *PLoS ONE* 19, no. 4 (2024): e0301132, https://doi.org/10.1371/journal.pone.0301132.
- 39. Ö. Çiçek, A. Abdulkadir, S. S. Lienkamp, T. Brox, and O. Ronneberger, 3D U-Net: Learning Dense Volumetric Segmentation from Sparse Annotation (Springer International Publishing, 2016), 424–432.
- 40. B. B. Avants, N. J. Tustison, M. Stauffer, G. Song, B. Wu, and J. C. Gee, "The Insight ToolKit Image Registration Framework," *Frontiers in Neuroinformatics* 8 (2014): 44, https://doi.org/10.3389/fninf.2014.00044.
- 41. M. McCormick, X. Liu, J. Jomier, C. Marion, and L. Ibanez, "ITK: Enabling Reproducible Research and Open Science," *Frontiers in Neuroinformatics* 8 (2014): 13, https://doi.org/10.3389/fninf.2014.00013.
- 42. P. M. Johnson, R. Taylor, T. Whelan, J. D. Thiessen, U. Anazodo, and M. Drangova, "Rigid-Body Motion Correction in Hybrid PET/MRI Using Spherical Navigator Echoes," *Physics in Medicine and Biology* 64, no. 8 (2019): 08nt03, https://doi.org/10.1088/1361-6560/ab10b2.
- 43. M. A. Griswold, P. M. Jakob, R. M. Heidemann, et al., "Generalized Autocalibrating Partially Parallel Acquisitions (GRAPPA)," *Magnetic Resonance in Medicine* 47, no. 6 (2002): 1202–1210, https://doi.org/10.1002/mrm.10171.
- 44. X. Zong and W. Lin, "Quantitative Phase Contrast MRI of Penetrating Arteries in Centrum Semiovale at 7T," *NeuroImage* 195 (2019): 463–474, https://doi.org/10.1016/j.neuroimage.2019.03.059.

- 45. M. E. MacDonald, N. D. Forkert, G. B. Pike, and R. Frayne, "Phase Error Correction in Time-Averaged 3D Phase Contrast Magnetic Resonance Imaging of the Cerebral Vasculature," *PLoS ONE* 11, no. 2 (2016): e0149930, https://doi.org/10.1371/journal.pone.0149930.
- 46. D. A. Feinberg and A. S. Mark, "Human Brain Motion and Cerebrospinal Fluid Circulation Demonstrated With MR Velocity Imaging," *Radiology* 163, no. 3 (1987): 793–799, https://doi.org/10.1148/radiology. 163,3.3575734.
- 47. J. Martin Bland and D. Altman, "Statistical Methods for Assessing Agreement Between Two Methods of Clinical Measurement," *Lancet* 327, no. 8476 (1986): 307–310, https://doi.org/10.1016/S0140-6736(86) 90837-8.
- 48. J. Moore, J. Jimenez, W. Lin, W. Powers, and X. Zong, "Prospective Motion Correction and Automatic Segmentation of Penetrating Arteries in Phase Contrast MRI at 7 T," *Magnetic Resonance in Medicine* 88, no. 5 (2022): 2088–2100, https://doi.org/10.1002/mrm.29364.
- 49. X. Zong, S. Nanavati, S.-C. Hung, T. Li, and W. Lin, "Effects of Motion and Retrospective Motion Correction on the Visualization and Quantification of Perivascular Spaces in Ultrahigh Resolution T2-Weighted Images at 7T," *Magnetic Resonance in Medicine* 86, no. 4 (2021): 1944–1955, https://doi.org/10.1002/mrm.28847.
- 50. O. Balédent, M. C. Henry-Feugeas, and I. Idy-Peretti, "Cerebrospinal Fluid Dynamics and Relation With Blood Flow: A Magnetic Resonance Study With Semiautomated Cerebrospinal Fluid Segmentation," *Investigative Radiology* 36, no. 7 (2001): 368–377, https://doi.org/10.1097/00004424-200107000-00003.
- 51. W. Huijbers, K. R. A. Van Dijk, M. M. Boenniger, R. Stirnberg, and M. M. B. Breteler, "Less Head Motion During MRI Under Task Than Resting-State Conditions," *NeuroImage* Feb 15, 147 (2017): 111–120, https://doi.org/10.1016/j.neuroimage.2016.12.002.
- 52. S. Maknojia, N. W. Churchill, T. A. Schweizer, and S. J. Graham, "Resting State fMRI: Going Through the Motions," *Frontiers in Neuroscience* 13 (2019): 825, https://doi.org/10.3389/fnins.2019.00825.
- 53. S. Kato, E. Bagarinao, H. Isoda, et al., "Effects of Head Motion on the Evaluation of Age-Related Brain Network Changes Using Resting State Functional MRI," *Magnetic Resonance in Medical Sciences* 20, no. 4 (2021): 338–346, https://doi.org/10.2463/mrms.mp.2020-0081.
- 54. M. W. Brightman, "The Distribution Within the Brain of Ferritin Injected Into Cerebrospinal Fluid Compartments. I. Ependymal Distribution," *Journal of Cell Biology* 26, no. 1 (1965): 99–123, https://doi.org/10.1083/jcb.26.1.99.
- 55. M. W. Brightman, "The Distribution Within the Brain of Ferritin Injected into Cerebrospinal Fluid Compartments. II. Parenchymal Distribution," *American Journal of Anatomy* 117, no. 2 (1965): 193–219, https://doi.org/10.1002/aja.1001170204.
- 56. H. Lee, L. Xie, M. Yu, et al., "The Effect of Body Posture on Brain Glymphatic Transport," *Journal of Neuroscience* 35, no. 31 (2015): 11034–11044, https://doi.org/10.1523/jneurosci.1625-15.2015.
- 57. R. C. Martin-Du Pan, R. Benoit, and L. Girardier, "The Role of Body Position and Gravity in the Symptoms and Treatment of Various Medical Diseases," *Swiss Medical Weekly* 134, no. 37–38 (2004): 543–551, https://doi.org/10.4414/smw.2004.09765.
- 58. J. J. Iliff, M. Wang, D. M. Zeppenfeld, et al., "Cerebral Arterial Pulsation Drives Paravascular CSF-Interstitial Fluid Exchange in the Murine Brain," *Journal of Neuroscience* 33, no. 46 (2013): 18190–18199, https://doi.org/10.1523/JNEUROSCI.1592-13.2013.
- 59. B. Pump, U. Talleruphuus, N. J. Christensen, J. Warberg, and P. Norsk, "Effects of Supine, Prone, and Lateral Positions on Cardiovascular and Renal Variables in Humans," *American Journal of Physiology. Regulatory, Integrative and Comparative Physiology* 283, no. 1 (2002): R174–R180, https://doi.org/10.1152/ajpregu.00619.2001.

- 60. J. Højlund, M. Sandmand, M. Sonne, et al., "Effect of Head Rotation on Cerebral Blood Velocity in the Prone Position," *Anesthesiology Research and Practice* 2012 (2012): 647258, https://doi.org/10.1155/2012/647258.
- 61. S. Dharmavaram, W. S. Jellish, R. P. Nockels, et al., "Effect of Prone Positioning Systems on Hemodynamic and Cardiac Function During Lumbar Spine Surgery: An Echocardiographic Study," *Spine (Phila Pa 1976)* 31, no. 12 (2006): 1388–1393, https://doi.org/10.1097/01.brs.00002 18485.96713.44.
- 62. S. Ogoh, K. Sato, K. Okazaki, et al., "Blood Flow in Internal Carotid and Vertebral Arteries During Graded Lower Body Negative Pressure in Humans," *Experimental Physiology* 100, no. 3 (2015): 259–266, https://doi.org/10.1113/expphysiol.2014.083964.
- 63. D. H. Spodick, A. P. Flessas, and S. Kumar, "Effect of the Prone Position on the Phases of the Cardiac Cycle," *Chest* 59, no. 3 (1971): 352–354, https://doi.org/10.1378/chest.59.3.352.
- 64. I. A. Fernandes, J. D. Mattos, M. O. Campos, et al., "Selective α 1-Adrenergic Blockade Disturbs the Regional Distribution of Cerebral Blood Flow During Static Handgrip Exercise," *American Journal of Physiology. Heart and Circulatory Physiology* 310, no. 11 (2016): H1541–H1548, https://doi.org/10.1152/ajpheart.00125.2016.
- 65. L. Yang, B. T. Kress, H. J. Weber, et al., "Evaluating Glymphatic Pathway Function Utilizing Clinically Relevant Intrathecal Infusion of CSF Tracer," *Journal of Translational Medicine* 11 (2013): 107, https://doi.org/10.1186/1479-5876-11-107.
- 66. B. Bedussi, M. Almasian, J. de Vos, E. VanBavel, and E. N. Bakker, "Paravascular Spaces at the Brain Surface: Low Resistance Pathways for Cerebrospinal Fluid Flow," *Journal of Cerebral Blood Flow and Metabolism* 38, no. 4 (2018): 719–726, https://doi.org/10.1177/0271678x17737984.
- 67. J. E. Kang, M. M. Lim, R. J. Bateman, et al., "Amyloid-Beta Dynamics Are Regulated by Orexin and the Sleep-Wake Cycle," *Science* 326, no. 5955 (2009): 1005–1007, https://doi.org/10.1126/science.1180962.
- 68. M. M. Laganà, S. J. Shepherd, P. Cecconi, and C. B. Beggs, "Intracranial Volumetric Changes Govern Cerebrospinal Fluid Flow in the Aqueduct of Sylvius in Healthy Adults," *Biomedical Signal Processing and Control* 36 (2017): 84–92, https://doi.org/10.1016/j.bspc.2017.03.019.
- 69. N. Aristokleous, I. Seimenis, Y. Papaharilaou, et al., "Effect of Posture Change on the Geometric Features of the Healthy Carotid Bifurcation," *IEEE Transactions on Information Technology in Biomedicine* 15, no. 1 (2011): 148–154, https://doi.org/10.1109/titb.2010.2091417.

Supporting Information

Additional supporting information can be found online in the Supporting Information section. Figure S1: The 3D U-Net architecture used for CAq segmentation. Figure S2: Threshold based ROI definitions for CAq, VA, ICA, IJV, SSS, and SRS. In each panel, the left image shows the original magnitude image, and the right image displays outer boundaries of the generated vessel masks (dark blue) and ringshaped background (light blue) ROIs. Figure S3: (A)-(C) The three visual cues designed for performing three different head movement types: roll, pitch, and yaw. Green arrows indicate the motion direction of the red fixation mark. (D)-(F) depict the expected motion paradigms during the experiment. Figure S4: (A) illustrates the head position of the subject in the supine posture. (B, C) illustrate the head positions in the prone posture; only one of these positions was used during the actual scan. Figure S5: Representative PC-MRI images of the cervical vessels acquired under three conditions: still, head motion with PMC, and head motion without PMC in two subjects. Blue boxes indicate the boundary of the enlarged views displayed adjacent to each image to highlight the VA/ICA/IJV at the center. Figure S6: Motion traces from two scans of VA/ICA/IJV with and without PMC during which the subject performed instructed head movement. These traces correspond to

the vascular scans shown in Figure 5S(A). Figure S7: Motion traces from two scans of VA/ICA/IJV with and without PMC during which the subject performed instructed head movement. These traces correspond to the vascular scans shown in Figure 5S(B). Figure S8: Motion traces from two scans of CAq with and without PMC during which the subject performed instructed head movement. These traces correspond to the vascular scans shown in Figure 8(A). Figure S9: Motion traces from two scans of CAq with and without PMC during which the subject performed instructed head movement. These traces correspond to the vascular scans shown in Figure 8(B). Figure S10: Motion traces from two scans of SSS/SRS with and without PMC during which the subject performed instructed head movement. These traces correspond to the vascular scans shown in Figure 9(A). Figure S11: Motion traces from two scans of SSS/SRS with and without PMC during which the subject performed instructed head movement. These traces correspond to the vascular scans shown in Figure 9(A). Figure S12: (A-C) show the relationships between motion-induced changes in Fabs in the CAq, SSS, and SRS and the motion scores. (D-F) show the corresponding relationships between motion induced changes in Vrange in CAq or mean blood flow velocity in the SSS and SRS and the motion scores.